Phase classification in the long-range Harper model using machine learning

Aamna Ahmed,[1,*] Abee Nelson,[1,*] Ankur Raina,[2] and Auditya Sharma[1]
[1]*Department of Physics, Indian Institute of Science Education and Research, Bhopal, Madhya Pradesh 462066, India*
[2]*Department of EECS, Indian Institute of Science Education and Research, Bhopal, Madhya Pradesh 462066, India*

(Received 27 April 2023; revised 4 September 2023; accepted 28 September 2023; published 18 October 2023)

In this work, we map the phase diagrams of one-dimensional quasiperiodic models using artificial neural networks. We observe that the multiclass classifier precisely distinguishes the various phases, namely the delocalized, multifractal, and localized phases, when trained on the eigenstates of the long-range Aubry-André Harper (LRH) model. Additionally, when this trained multilayer perceptron is fed with the eigenstates of the Aubry-André Harper (AAH) model, it identifies various phases with reasonable accuracy. We examine the resulting phase diagrams produced using a single disorder realization and demonstrate that they are consistent with those obtained from the conventional method of fractal dimension analysis. Interestingly, when the neural network is trained using the eigenstates of the AAH model, the resulting phase diagrams for the LRH model are less exemplary than those previously obtained. Further, we study binary classification by training the neural network on the probability density corresponding to the delocalized and localized eigenstates of the AAH model. We are able to pinpoint the critical transition point by examining the metric "accuracy" for the central eigenstate. The effectiveness of the binary classifier in identifying a previously unknown multifractal phase is then evaluated by applying it to the LRH model.

DOI: 10.1103/PhysRevB.108.155128

I. INTRODUCTION

The application of machine learning (ML) techniques in the field of condensed matter physics has been a subject of great interest in recent times [1]. This interdisciplinary field has rapidly gained popularity owing to the advantages presented by machine learning [2–4]. As an actively evolving area of research, ML techniques have been used to detect classical and quantum phase transitions [5–13], for the acceleration of Monte Carlo simulations [14–16], and for representation of states of quantum many-body systems [17–25]. A popular subcategory of machine learning is supervised learning [26], where one trains algorithms to utilize labeled training data sets in order to classify new data or make predictions accurately. This motivates its application in condensed matter physics for classifying various phases in strongly correlated systems [5,27], topological systems [28–30], and quantum many-body systems [9,17].

Disordered quantum systems [31–36] have been a fascinating topic of study for a long time. In the 1D Anderson model [31], the tiniest of disorder is known to localize single-particle states exponentially. In contrast, the Aubry-Andrè-Harper (AAH) [37,38] model, governed by a quasiperiodic disorder, exhibits a delocalization-localization transition even in one dimension. Interestingly, instead of the exponential localization observed in the short-ranged model, the eigenstates show algebraic localization [39–41] in the case of long-range hopping. This has naturally led to exciting studies exploring the effects of quasiperiodic disorder in long-range systems [42,43].

The interplay of power-law hopping $(1/r^{\sigma})$ and the quasiperiodic potential results in a rich structure [42] in the single-particle eigenstates. The self-duality of the quasiperiodic AAH model is broken, and mobility edges are observed when the hopping is no longer restricted to nearest neighbors only. While multifractal eigenstates are observed to coexist with delocalized eigenstates for $\sigma < 1$, localized states exist together with delocalized eigenstates for $\sigma > 1$ [42]. The localization characteristics of these single-particle eigenstates have been determined [42,44] with the aid of several well-known measures, such as fractal dimension [45,46], inverse participation ratio [47,48], level spacing [49], and many more. These methods depend on a physical understanding of the nature of the regime.

In the present work, we construct a neural network for characterizing the phase diagram beyond established methods in single-particle Hamiltonian models. We study the one-dimensional long-range AAH (LRH) model, where multifractal (localized) eigenstates can coexist with delocalized eigenstates for the long-range hopping parameter $\sigma < 1$ ($\sigma > 1$). The information required for classifying the delocalized, localized, and multifractal regimes is obtained from the eigenstates which are used as inputs to the neural network. The trained network is first used to classify all the eigenstates of the LRH model for various values of the hopping parameter σ. We then consider the case of $\sigma \to \infty$, i.e., the standard AAH model, and classify its eigenstates as delocalized/localized/multifractal. We show that the phase diagram obtained by feeding a single disorder realization in the neural network is in good agreement with results obtained

[*]These authors contributed equally to this work.

using conventional methods. We next train the same network using the eigenstates of the AAH model. In this case, although the network can identify the localized phase accurately, some discrepancy is seen in the case of multifractal and delocalized states. We also utilize binary classification to identify the transition point of the AAH model by training the neural network on its delocalized and localized eigenstates. While this network precisely identifies the phase diagram for the AAH model, it can also identify the multifractal phase (for which no explicit training is given) of the LRH model, although this is achieved only in a coarse manner.

This paper is organized as follows. Section II discusses the details of the Hamiltonian model and carries an introduction to the general setup of the neural network. In Sec. III, we discuss the network architecture used for the classification as well as the details of the input data. In Sec. IV, we present our multiclass and binary classification results and compare them against the results obtained through a conventional method. We then summarize our results in Sec. V. The utilization of the binary classifier trained on the data of a 1D model to predict the phase diagram of a 3D model is discussed in Appendix A.

II. MODEL AND METHODS

A. Hamiltonian

We consider the one-dimensional long-range Harper (LRH) model given by the Hamiltonian

$$\hat{H} = -\sum_{i<j}^{N}\left(\frac{J}{r_{ij}^{\sigma}}\hat{c}_i^{\dagger}\hat{c}_j + \text{H.c.}\right) + \lambda\sum_{i=1}^{N}\cos(2\pi\alpha i + \theta_p)\hat{c}_i^{\dagger}\hat{c}_i, \tag{1}$$

where $\hat{c}_i^{\dagger}$ ($\hat{c}_i$) represents the single-particle creation (destruction) operator at site i. The first term describes hopping, where $r_{ij} = (N/\pi)\sin(\pi|i-j|/N)$ is the geometric distance between the sites i and j in a ring. The strength of the long-range hopping is controlled by J, which we set to unity and the long-range parameter in the hopping, namely σ. The second term describes the quasiperiodic on-site energy, where the strength of the quasiperiodic potential is λ, and the quasiperiodicity parameter α is taken to be an irrational number, set as the golden mean $(\sqrt{5}-1)/2$ [50]. θ_p is an arbitrary global phase chosen randomly from a uniform distribution in the $[0, 2\pi]$ range. The total number of sites is N, and periodic boundary conditions are assumed. In the limit $\sigma \to \infty$, the hopping is effectively nearest neighbor, and we recover the standard AAH model [37,38]:

$$\hat{H} = -J\sum_{i=1}^{N}(\hat{c}_i^{\dagger}\hat{c}_{i+1} + \text{H.c.}) + \sum_{i=1}^{N}\lambda\cos(2\pi\alpha i + \theta_p)\hat{c}_i^{\dagger}\hat{c}_i. \tag{2}$$

It is well known [50] that all the energy eigenstates are delocalized when $\lambda < 2$, and all the energy eigenstates are localized when $\lambda > 2$. $\lambda = 2$ is the critical point where all the eigenstates are multifractal [51]. It is known that the AAH model is self-dual [37,52]; at the critical point $\lambda = 2$, the AAH model in position space maps to itself in momentum space. When long-range hopping is introduced (σ is finite), the self-duality condition is broken.

B. Artificial neural network

The artificial neural network (ANN) is inspired by the neuronal network in the biological brain [53,54]. The ANN combines a series of linear maps and nonlinear functions [55] that are successively applied to the input data in order to obtain the final output. A mapping defines each layer of the network, and the dimension of a layer corresponds to the number of neurons in it. In this work, in the case of multiclass classification, we utilize vectors $\{x\}$ of dimension m_1 and train a map $f(x)$ to map them to the *target set* $\{(0,0,1),(0,1,0),(1,0,0)\}$. One-hot vectors represent this target set and deliver the final output in the form of entries of the neurons of the output layer. The network is trained on a data set called the *training set*, and its performance is gradually improved by adjusting its parameters. In supervised learning, the training set consists of labeled data; i.e., for each input x, the output is already known to map to one of the outcomes of the target set. The trained network then classifies previously unseen data from the *testing set*.

We next describe the functioning of the neural network. The "input layer" maps the initial vectors of dimension m_1 to a space of dimension m_2 with the help of a linear map and a nonlinear *activation function* A [56]. Subsequently, the mapping between the nth and the $(n+1)$th layer is defined as

$$x^{(n)} \mapsto x^{(n+1)} = A(W^{(n+1,n)}x^{(n)} + B^{(n+1)}). \tag{3}$$

Here matrix-vector multiplication is implied between $W^{(n+1,n)}$ (matrix of dimension $m_{n+1} \times m_n$) and $x^{(n)}$ (vector of dimension m_n). The resulting vector $x^{(n+1)}$ is a vector of dimension m_{n+1}. The elements of the matrix $W^{(n+1,n)}$ are called the *weights*, and the corresponding elements of the vector $B^{(n+1)}$ are called the *biases*. The final layer of the ANN is referred to as the "output layer," with the number of nodes equal to the number of expected outputs that the network is trained for. The layers between the input and output layers are called *hidden layers*, which can range from one to several. The method of training neural networks with multiple hidden layers is referred to as *deep learning* [57]. Also, if the number of neurons in a layer is huge, the network learns nonuniversal features and unnecessary details for classification. This can lead to *overfitting* of data. Thus in this study we employ dropout regularization [58] to avoid the gradual accumulation of neuronal weight configurations.

In the case of multiclass classification, the inputs to the network consist of the amplitudes of an eigenstate of the Hamiltonian of interest. For the hidden layers, we utilize the leaky rectified linear unit (ReLU) activation function [59], defined as

$$\text{leaky ReLU:}\quad f(x_i) = \begin{cases} 0.01x_i, & x_i < 0, \\ x_i, & x_i \geqslant 0. \end{cases} \tag{4}$$

In the output layer, we consider the softmax activation function [60], defined as

$$\text{softmax:}\quad f(x_i) = \frac{e^{-x_i}}{\sum_j e^{-x_j}}. \tag{5}$$

The softmax function estimates the output corresponding to each target set vector, which sums up to unity. These

TABLE I. The activation functions in the hidden/output layer of the multiclass and binary classifiers.

Neural network	Hidden layer activation function	Output layer activation function
Multiclass classifier	Leaky ReLU	Softmax
Binary classifier	ReLU	Sigmoid

projections can be interpreted as the confidence of the network to assign a class to the input data.

In the case of binary classification, since the probability densities are considered as inputs, we utilize the ReLU activation function [61]:

$$\text{ReLU:} \quad f(x_i) = \begin{cases} 0, & x_i < 0, \\ x_i, & x_i \geqslant 0, \end{cases} \tag{6}$$

in the hidden layers. In the output layer, we employ the sigmoid activation function [60], defined as

$$\text{sigmoid:} \quad f(x_i) = \frac{1}{1 + e^{-x_i}}, \tag{7}$$

to obtain a single output. There are two main advantages of the ReLU function: (a) it is computationally efficient as it only involves a simple comparison, and (b) it introduces nonlinearity in the model. On the other hand, the sigmoid function has a smooth and continuous output, which makes it easier to compute gradients during back-propagation and to optimize the model using gradient-based methods such as the stochastic gradient descent. The activation functions in the hidden and output layers of both the neural networks are compiled in Table I.

In order to correctly estimate various parameters such as the weights and biases, the network utilizes a loss/cost function [57] as well as an optimizer during the training process. The cost function measures the distance between the predicted outputs and their actual values. In general, cross entropy is widely used as a loss function when optimizing classification models. For classification problems, we utilize the cross-entropy loss function,

$$L_{\text{CE}} = \sum_{i=1}^{c_n} T_i \ln S_i, \tag{8}$$

where c_n denotes the number of classes, $\{S_i\}$ are the probabilities obtained from the softmax/sigmoid output layer, and $\{T_i\}$ are the true values, namely 0 or 1.

Another step involved in network training is back-propagation [62], where the weights and biases are adjusted in successive iterations to reduce the output of the loss function. The updating rate of the parameters is called the *learning rate*. This is done through the *gradient descent* optimization algorithm, which is computationally expensive. To overcome storage issues, the training data are broken down into small *batches*, which can be easily fed to the model. When all the training data are fed to the model in batches, this is called an *epoch*. Thus, every batch in the training data set can update the internal model parameters once during an epoch. In order for the model to learn the gradient or the direction it should take to minimize the loss function, we employ an adaptive learning rate optimizer *Adam* [63], which incorporates adaptive estimates of the gradients and their squares. The neural network evaluates the loss function on the training data set at the end of each epoch; this is known as the training loss [64]. An additional data set for validation is considered for every epoch to determine whether or not the network is fully trained, that is, whether it can generalize its knowledge to sets of previously unseen data. The neural network is then made to evaluate the loss function on the validation data set; this is known as the validation loss. The training and validation loss for a good fit should gradually reduce and converge to 0 as the number of epochs increases.

III. NEURAL NETWORK APPROACH

We perform exact diagonalization on the Hamiltonian to obtain the single-particle eigenstates. Our goal is to be able to build an effective neural network that can classify these eigenstates according to their localization properties. We build and analyze two neural networks: a multiclass and a binary classification network. While the amplitudes of the eigenstates are utilized as inputs for the multiclass classification network, the on-site probability densities drawn from the eigenstates are taken to be the inputs in the case of the binary classification network. We discuss both cases in detail below.

A. Multiclass classification

We consider a system with $N = 510$ sites, and obtain the single-particle eigenstates of the LRH model [44] given by Eq. (1). We then generate the training data by varying the disorder strength λ in small steps (0.02) in the range of 0–5 for the long-range hopping parameter strengths $\sigma = 0.5, 1.5$, and 3 for several disorder samples. As mentioned earlier, the multifractal (localized) eigenstates coexist with delocalized eigenstates for $\sigma < 1$ ($\sigma > 1$) in the LRH model; the chosen parameters help us to obtain data corresponding to all three classes, i.e., delocalized, multifractal, and localized.

In order to label the eigenstates required for network training, we calculate a well-known quantity called fractal dimension D_q [51,65,66] by coarse-graining the system into boxes of length l. Given a normalized wave function $|\psi_k\rangle = \sum_{i=1}^{N} \psi_k(i)|i\rangle$ defined over a lattice of size N, we divide the lattice into N/l segments of length l [67]. The fractal dimension is then defined as

$$D_q = \frac{1}{q-1} \frac{\ln \sum_{p=1}^{N/l} \left[\sum_{i=(p-1)l+1}^{pl} |\psi_k(i)|^{2q} \right]}{\ln[l/N]}. \tag{9}$$

The fractal dimension in the limit $N \to \infty$ is given by [51]

$$D_q^{\infty} = \lim_{N \to \infty} D_q. \tag{10}$$

For a perfectly delocalized state, $D_q^{\infty} = 1$, while for a localized state, D_q^{∞} is vanishing, for all $q > 0$. For intermediate cases, $0 < D_q^{\infty} < 1$, which is a sign that the state is multifractal.

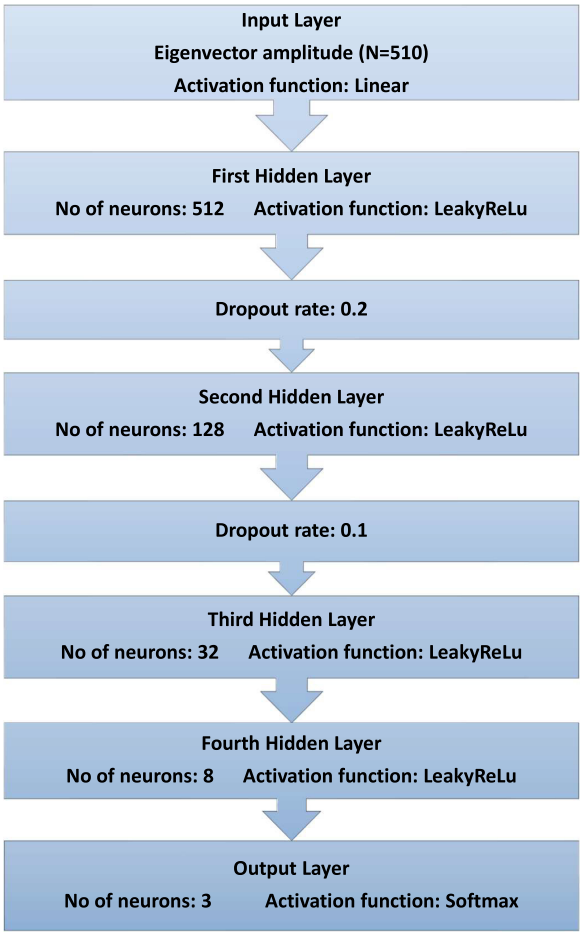

FIG. 1. A schematic diagram of the neural network architecture for multiclass classification of eigenstates. Here the input layer is equal to system size N, and the output layer has 3 neurons, which gives the confidence of the state being delocalized, multifractal, and localized. Nonlinearities are introduced by the leaky rectified linear unit (leaky ReLU). Dropout is included to increase classification accuracy.

Here for each eigenstate, we calculate the fractal dimension D_2 and label it as follows:

$$\begin{aligned} D_2 &< 0.2, && \text{localized}, \\ 0.2 \leqslant D_2 &\leqslant 0.8, && \text{multifractal}, \\ D_2 &> 0.8, && \text{delocalized}. \end{aligned} \tag{11}$$

We first generate a training data set comprising 300 000 eigenstates of the LRH model belonging to each of the three classes, by considering various values of σ, θ, and λ. A schematic flowchart to describe the complete architecture of the neural network performing multiclass classification is shown in Fig. 1. The network comprises an input layer, several hidden layers, and an output layer coupled to the linear, leaky ReLU, and softmax activation functions, respectively. We have also added dropout layers to the model to avoid overfitting. The cost function is cross entropy, and the neural network weights are optimized using the Adam optimizer. We consider batch sizes of 500 samples, which add up to 900 000 samples per epoch, with an 80%-20% split between

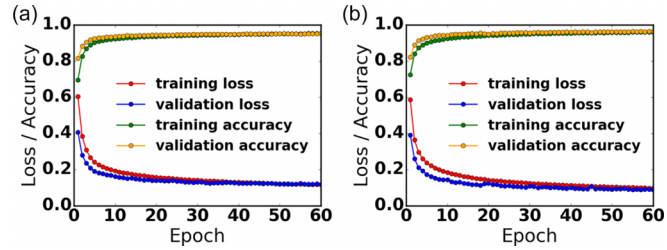

FIG. 2. The training loss and training accuracy along with the validation loss and validation accuracy versus the number of epochs for the neural network trained using eigenstates of the (a) LRH model and (b) AAH model. The stabilization in loss occurs around 50 epochs and beyond, indicating that the ANN is trained.

training and validation. We observe that fixing the number of training epochs to 60 allows us to obtain an accuracy of $\approx 95\%$ as shown in Fig. 2(a). Here accuracy is defined as the ratio of eigenstates correctly classified to the total number of eigenstates. Once the network is trained, the eigenvectors from each point in the phase space of (λ, σ) are fed to the network. We obtain three values each of which lies between 0 and 1 and corresponds to the neural network's confidence of classifying the given input in each phase/class.

We next generate another training data set comprising eigenstates of the AAH model given by Eq. (2). Once again the training set consists of 300 000 eigenstates belonging to each class classified as localized, multifractal, and delocalized using D_2 [see Eq. (11)]. The network architecture is the same as before (see Fig. 1). The neural network weights are tuned using an Adam optimizer, and the cost function is cross entropy, as before. Here again 60 training epochs have been considered, and the batch size is 500. The 80%-20% split between training and validation is followed once again. As demonstrated in Fig. 2(b), the network is trained to an accuracy of $\approx 95\%$.

B. Binary classification

For binary classification, we train the network using the on-site probability densities (PDs) of the delocalized and localized eigenstates of the AAH model. As mentioned earlier, all the eigenstates are delocalized (localized) below (above) a critical disorder strength $\lambda = 2$, at which the eigenstates show multifractal behavior. For a system size of $N = 510$, we consider 100 disorder realizations (θ_i) generating 51 000 samples separately for the delocalized and localized classes by choosing disorder strengths $\lambda = 0.5$ and 4, respectively. We construct a neural network which consists of an input layer of size N and utilizes on-site probability densities of the eigenstates as inputs. This is followed by a single hidden layer with the number of neurons equal to the greatest integer less than $[N \times (2/3)] + 1$. The neurons are coupled to the ReLU activation function and an output layer coupled to the sigmoid activation function. The single output obtained is a number that lies between 0 and 1; a value close to 0 indicates that the state is delocalized while a value close to 1 indicates that it is localized. The scheme of the neural network architecture is shown in Fig. 3. Here the cost function is binary cross entropy, and the optimizer is Adam. The batch size is 300

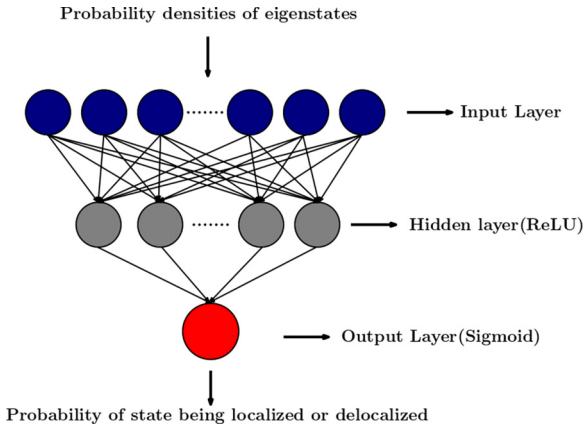

FIG. 3. Neural network architecture for binary classification of delocalized and localized eigenstates. Here nonlinearities are introduced by the rectified linear unit (ReLU).

samples, and 5 training epochs are considered; we find that this is sufficient to obtain an accuracy of $\approx 100\%$, when the training and validation data set is split into an 80 : 20 ratio. We use the metric "accuracy" to identify the phase transitions. By training on two phases only, we also examine the ability of the neural network to identify a previously unknown phase.

IV. RESULTS

In this section, we perform multiclass and binary classification using the eigenvectors and probability densities, respectively. The results obtained using the neural network approach are compared to the ones acquired from the conventional multifractal analysis of D_q.

A. Multiclass classification

We begin our analysis by calculating the multifractal dimension D_q as a function of disorder strength λ for all the single-particle eigenstates of the LRH Hamiltonian for $\sigma = 0.5$, 1.5, and 3.0 as shown in Figs. 4(a)–4(c), respectively. In the case of $\sigma = 0.5$, with an increase in disorder strength, the fraction of delocalized eigenstates decreases, and multifractal

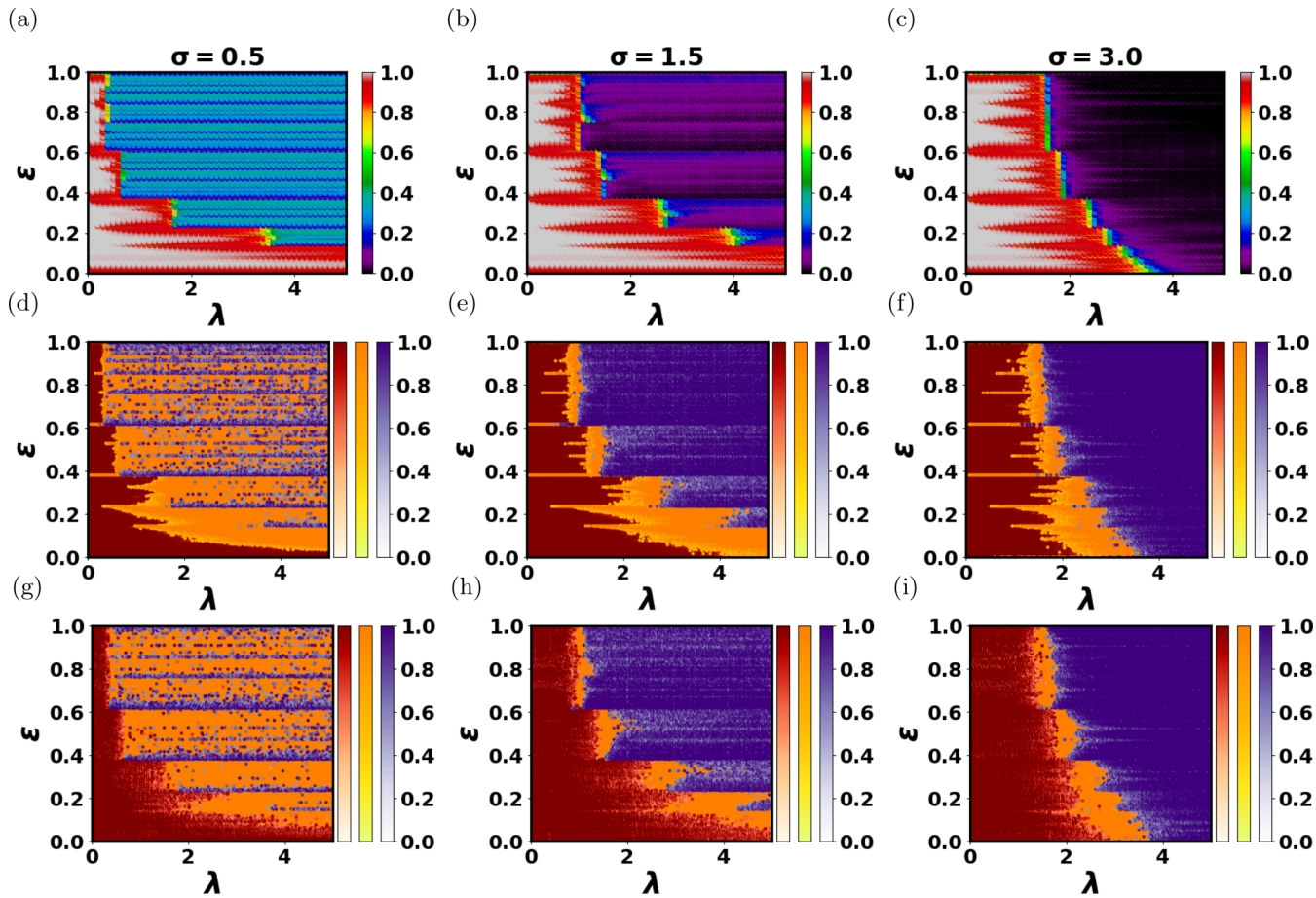

FIG. 4. Fractal dimension D_2 (whose value is represented by a color according to the code shown) as a function of disorder strength λ and for increasing fractional eigenstate index i/N starting from the ground state for the long-range hopping parameter σ equal to (a) 0.5, (b) 1.5, and (c) 3.0. Here averaging has been performed over 100 disorder realizations. Classification of the single disorder realization of the LRH model using the network trained on the eigenstates of the LRH model for hopping parameter σ equal to (d) 0.5, (e) 1.5, and (f) 3.0. Classification of the single disorder realization of the LRH model using the network trained on the eigenstates of the AAH model for hopping parameter σ (g) 0.5, (h) 1.5, and (i) 3.0. The color of each point (σ, λ) represents the confidence of the network for the delocalized (red), multifractal (orange), and localized (purple) phases. Here system size is $N = 510$ in all cases.

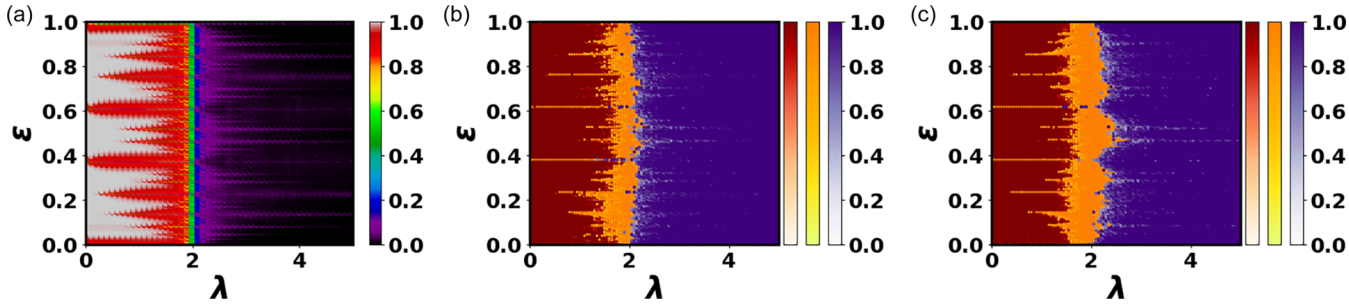

FIG. 5. Fractal dimension D_2 (whose value is represented by a color according to the code shown) as a function of disorder strength λ and increasing fractional eigenstate index i/N starting from the ground state. Here averaging has been performed over 100 disorder realizations. Classification of the single disorder realization of the eigenstates using the network trained on the eigenstates of the (b) LRH model and (c) AAH model. The color of each point indicates the confidence for the delocalized (red), multifractal (orange), and localized (purple) phases. Here system size $N = 510$ in all cases.

states are observed to appear in blocks, as shown in Fig. 4(a). Thus a delocalized-to-multifractal (DM) edge is observed in the eigenstate spectrum, which changes in a steplike fashion with increasing disorder strength λ. In the case of $\sigma = 1.5$ [see Fig. 4(b)] and $\sigma = 3.0$ [see Fig. 4(c)], we observe that the delocalized eigenstates are separated from the localized eigenstates, with a delocalized-to-localized (DL) edge which changes in a steplike fashion as the number of delocalized states decreases with increasing disorder strength λ. We also observe the presence of multifractal states in the vicinity of the DM/DL edges.

We next employ the multiclass classification algorithm for a single disorder realization and compare its performance with the multifractal analysis. First, the network (see Fig. 1) is trained using the eigenstates of the LRH model generated over multiple disorder realizations for various values of (σ, λ). We assign the class to the vectors in the training data set with the help of D_2 using Eq. (11). The phase diagram obtained as a function of disorder strength λ using the neural network for a single disorder realization is shown in Figs. 4(d)–4(f) corresponding to $\sigma = 0.5$, 1.5, and 3 respectively. The states are classified as delocalized, multifractal, and localized with confidence p_1, p_2, and p_3, respectively. In all figures, we have plotted the $\max(p_1, p_2, p_3)$ where the red, orange, and purple color codes are used to represent p_1, p_2, and p_3, respectively. Comparing Figs. 4(a)–4(c) with Figs. 4(d)–4(f), we observe that the shape and location of the transitions agree very well at all values of σ.

Next, we compare the neural-network-based transition characterization when the same network (see Fig. 1) is trained using the eigenstates of the AAH model. Although the existence of a critical disorder strength at which all eigenstates are multifractal and separate the delocalized and localized eigenstates is well known, we still assign the class to the vectors in the training data set with the help of D_2 using Eq. (11). Once the network is trained, we utilize it to obtain the phase diagrams of the LRH model as a function of disorder strength λ using the neural network for a single disorder realization as shown in Figs. 4(g)–4(i) corresponding to $\sigma = 0.5$, 1.5, and 3 respectively. While the network can precisely predict the location of the transitions/steps, the distinction between the delocalized and multifractal states is not very sharp. Nevertheless, we still observe the steplike features and the distinct phases.

We next compute the multifractal dimension D_q as a function of disorder strength λ for all the single-particle eigenstates of the AAH model [see Fig. 5(a)]. All the eigenstates are delocalized for $\lambda < 2$ while all eigenstates are localized for $\lambda > 2$. At $\lambda = 2$, the eigenstates are multifractal [50,51]. We obtain the phase diagram of the AAH model using the neural network trained on the eigenstates of the LRH model [see Fig. 5(b)] and the eigenstates of the AAH model [see Fig. 5(c)]. The neural network can accurately predict the phase diagram using a single disorder realization in both cases. We also checked that a network trained with a higher-order fractal dimension like D_6 is also able to faithfully reproduce the phase diagram as shown in Appendix B.

B. Binary classification

In this subsection, we discuss the results obtained with a binary classifier using the neural network shown in Fig. 3. The training data set consists of the probability densities (PDs) corresponding to the eigenstates of the two classes, i.e., delocalized ($\lambda = 0.5$) and localized ($\lambda = 4$). Since we have a

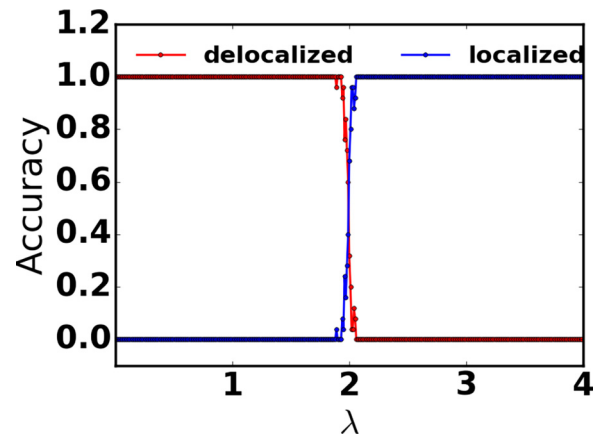

FIG. 6. Neural network classification accuracy with increasing disorder strength λ for the central eigenstate of the AAH model for system size $N = 510$ averaged over 25 disorder realizations.

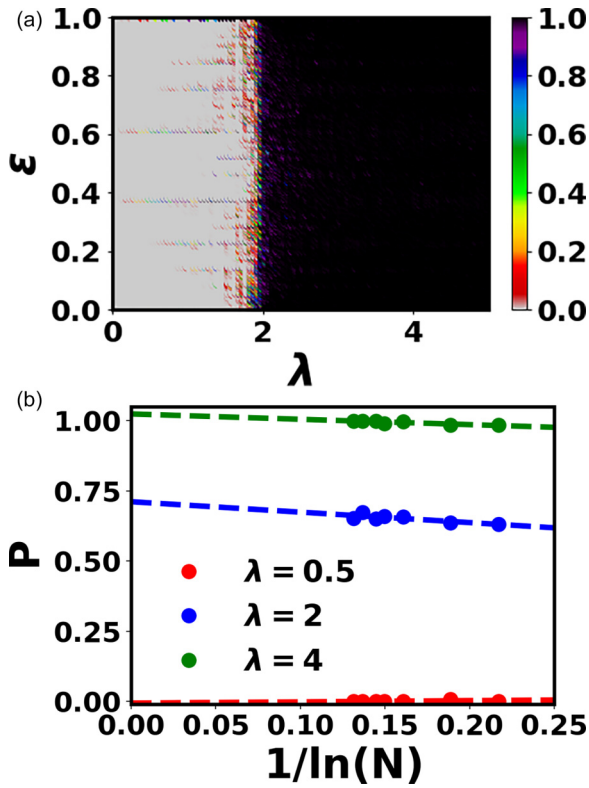

FIG. 7. (a) Classification of the eigenstates for a single disorder realization of the AAH model as a function of disorder strength λ and for increasing fractional eigenstate index i/N starting from the ground state. Here the network is trained on the delocalized ($\lambda = 0.5$) and localized eigenstates ($\lambda = 4$) of the AAH model. The probability of the state being localized is given by the single output P, whose value is represented by a color according to the code shown. The corresponding plot using fractal dimension D_q is shown in Fig. 5(a). Here system size is $N = 510$. (b) The probability P of the state being localized vs $\frac{1}{\ln(N)}$ in the delocalized phase $\lambda = 0.5$, at the critical point $\lambda = 2$ and in the localized phase with $\lambda = 4$. Here, system sizes range from $N = 100$ to $N = 2000$.

single neuron in the output layer, the output represents the probability P of the state being localized, implying that $1 - P$ is the probability of the state being delocalized. We may infer that intermediate values of P indicate that the state exhibits multifractal nature.

The information about the transition from the delocalized to localized regimes is incorporated in the properties of the eigenstates. We feed the central eigenstate (corresponding to the energy $E_{N/2}$ of the spectrum) to the trained network to determine the transition point. In Fig. 6, we have plotted the classification prediction as a function of disorder strength λ. The transition point is revealed to be at $\lambda = 2$ as the network learns the difference between the localized and delocalized eigenstates. The transition point obtained agrees with the one shown using multifractal dimension D_2 in Fig. 5(a).

Next, we test this trained neural network, by inputting the probability densities drawn from all the eigenstates of the AAH model, as λ is varied across the transition. The neural network gives a single output P, which signifies the confidence of the network to classify the state as localized, indicating that $1 - P$ is the probability of classifying the state as delocalized. For a single disorder realization, the phase diagram obtained from the neural network shown in Fig. 7(a) is consistent with the one obtained using multifractal dimension D_2 as shown in Fig. 5(a). We also note that at the transition point where the multifractal states exist, the prediction P lies roughly midway between 1 and 0, consistent with theoretical results. In Fig. 7(b), we numerically study the system-size dependence [35] of the probability P of the eigenstates being localized obtained using the binary classifier. While in the delocalized phase at $\lambda = 0.5$, P remains close to 0, at the multifractal point $\lambda = 2$, it lies between 0 and 1. In the localized phase with $\lambda = 4$, P approaches unity. This analysis is consistent with the ones obtained using conventional methods and can be utilized in classifying phases robustly against increasing system sizes.

Next, we implement the binary classification algorithm on the LRH model to investigate how well our neural network can identify a previously unknown phase. Since the network is trained exclusively on the delocalized and localized phases, it is unfamiliar with the multifractal regime. In Figs. 8(a)–8(c), we have plotted the phase diagram by feeding the eigenstates of a single disorder realization of the LRH model to the binary classifier corresponding to $\sigma = 0.5$, 1.5, and 3.0, respectively. We observe that our network can indicate the presence of a new phase (multifractal phase). In Fig. 8(a), for $\sigma = 0.5$, while the network shows confusion in the multifractal phase, the steplike features that distinctly separate the delocalized states can still be observed. In Figs. 8(b) and 8(c), for $\sigma = 1.5$ and 3.0, we observe that the delocalized and localized states are classified and separated by steplike edges along which multifractal states are observed with $0 < P < 1$. In other words, while the network identifies the delocalized and localized phases, in the case of the multifractal phase, it cannot clearly distinguish it from the localized phase. This inability of the network to produce results similar to multiclass classification is expected; as a matter of fact, the close connection between the phase diagram obtained by the binary classifier to the actual one is quite remarkable.

V. CONCLUSION

In this work, we explore the ability of artificial neural networks to extract information about various phases from single-particle states. We build a multilayer perceptron network and employ it to classify the delocalized, multifractal, and localized phases of the quasiperiodic long-range Harper model. Our neural network produces phase diagrams that align with theoretical predictions after being trained using the data associated with the three phases. We establish that the machine successfully learns each phase's property from the eigenstates. The machine has high confidence throughout all the phases, which is an indication of good feature extraction.

We also build a binary classifier with a single hidden layer having probability densities of the eigenstates of the AAH model as inputs to identify the delocalized and localized regimes. When we test this neural network with the AAH model, we find that the resulting phase diagram agrees very closely with the theoretically known phase diagram. Even though the network is not trained with multifractal states,

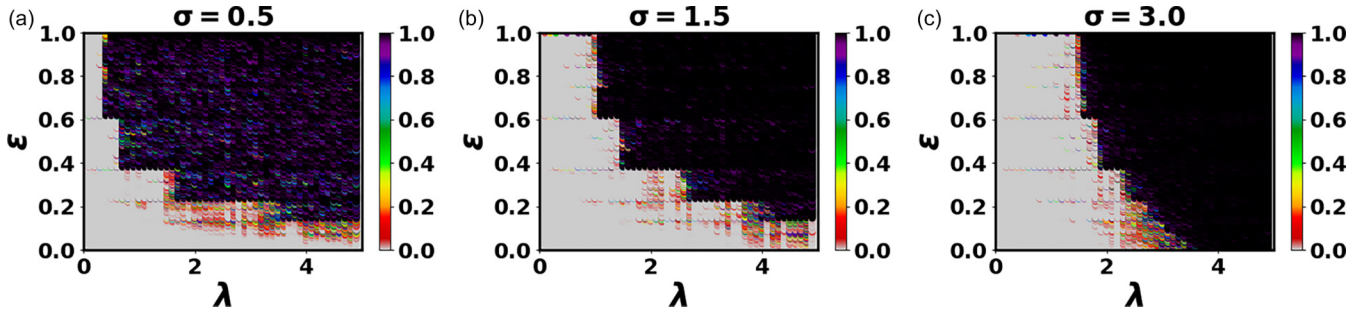

FIG. 8. Classification of the eigenstates for a single disorder realization of the LRH model as a function of disorder strength λ and with increasing fractional eigenstate index i/N starting from the ground state for the long-range hopping parameter σ equal to (a) 0.5, (b) 1.5, and (c) 3.0. Here the network is trained on the delocalized ($\lambda = 0.5$) and localized eigenstates ($\lambda = 4$) of the AAH model. The probability of the state being localized is given by the single output P, whose value is represented by a color according to the code shown. The corresponding plot using fractal dimension D_q is shown in Figs. 4(a)–4(c). Here system size is $N = 510$ in all cases.

the phase diagram obtained indicates the presence of multifractal states, in a manner very similar to the actual phase diagram. Subsequently, the network is applied to the LRH model for detecting an unlearned phase. The neural network shows confusion, whenever multifractal states are involved; however the phase diagram obtained is remarkably close to the actual one. In this work, we can obtain the phase diagrams with reasonable accuracy by feeding a single disorder realization to the trained neural network. Thus, the neural network method provides an alternative to the known conventional methods. Also, in recent times several works have explored the implementation of machine learning techniques in the context of many-body quantum systems [6,17,20,23–25]. A possible extension of our current work would be to identify and distinguish various phases in the many-body interacting system once the neural network learns the characteristics of the many-body wave functions in the different phases.

The phase classification problems in the literature have primarily focused on binary classification. In this context, investigating multiple phase transitions and training partially blind networks to recognize unknown phases remains unexplored. The value of this multineuron output strategy will be much more significant when dealing with novel phases for which acceptable order parameters are not known in advance.

ACKNOWLEDGMENTS

A.A. is grateful to the Council of Scientific and Industrial Research (CSIR), India, for support through her Ph.D. fellowship. A.S. acknowledges financial support from SERB via Grant No. CRG/2019/003447 and DST via DST-INSPIRE Faculty Award No. DST/INSPIRE/04/2014/002461. All neural networks used in this work were implemented in Python using TENSORFLOW [68].

APPENDIX A: 3D ANDERSON MODEL

In this section, we employ the binary classifier to plot the phase diagram of the 3D Anderson model [31]. In particular, we train the neural network (shown in Fig. 3) by utilizing the eigenstate probabilities of the 1D AAH model [Eq. (2)] with $N = 512$ sites. Since the dimension of the neural network's input layer is 512, we consider a cubic lattice with $8^3 = 512$ sites to obtain the network's prediction. The Hamiltonian of the 3D Anderson model is

$$\hat{H} = J \sum_{\langle i,j \rangle} (\hat{c}_i^\dagger \hat{c}_j + \text{H.c.}) + \Delta \sum_{i=1} \epsilon_i \hat{c}_i^\dagger \hat{c}_i, \qquad \text{(A1)}$$

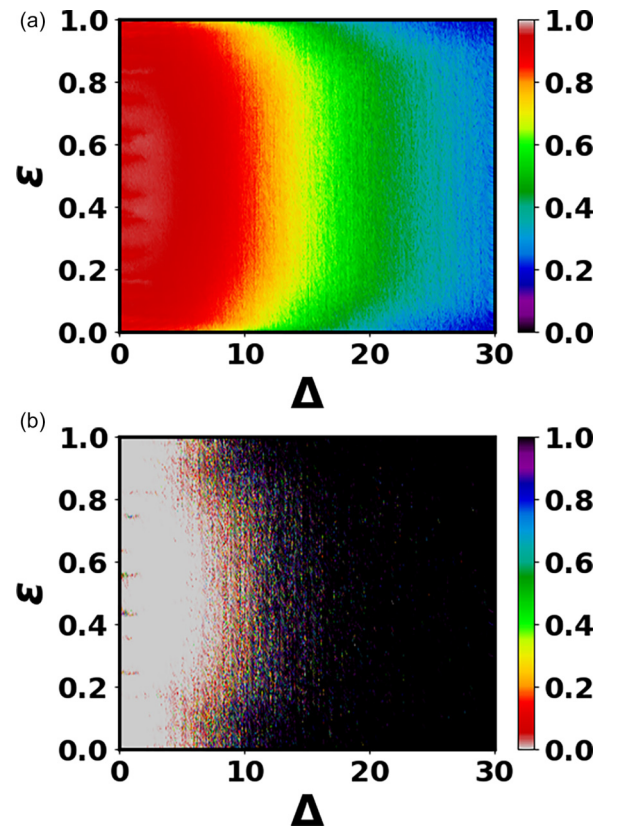

FIG. 9. (a) Fractal dimension D_2 (whose value is represented by a color according to the code shown) as a function of disorder strength Δ and increasing fractional eigenstate index i/N starting from the ground state for the 3D Anderson model. Here, averaging has been performed over 100 disorder realizations. (b) Classification of the eigenstates using the network trained on the central eigenstates of the AAH model of system size $N = 512$. The probability of the state being localized is given by the single output P, whose value is represented by a color according to the code shown. Here, the system size of the 3D Anderson model is $8^3 = 512$.

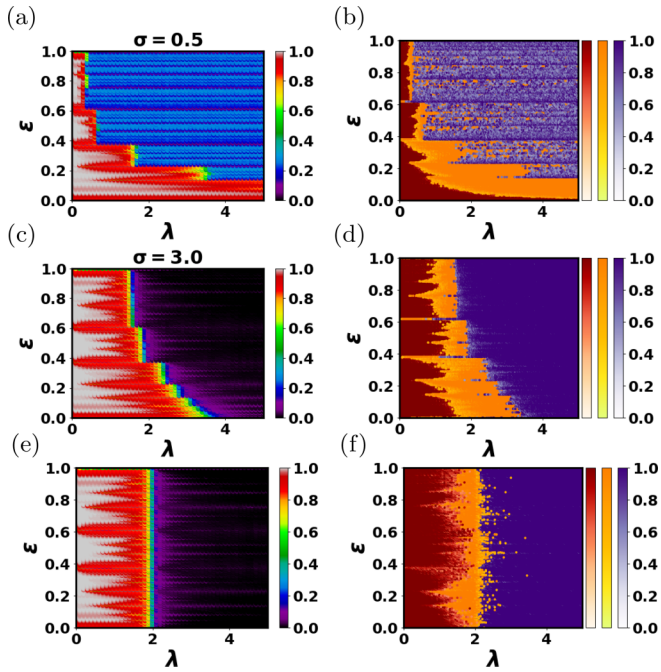

FIG. 10. Fractal dimension D_6 (whose value is represented by a color according to the code shown) as a function of disorder strength λ and for increasing fractional eigenstate index i/N starting from the ground state for the long-range hopping parameter σ equal to (a) 0.5, (c) 3.0, and (e) AAH model. Here, averaging has been performed over 100 disorder realizations. Classification of the single disorder realization of the LRH model using the network trained on the eigenstates of the LRH model for hopping parameter σ equal to (b) 0.5, (d) 3.0, and (f) AAH model. The color of each point (σ, λ) represents the confidence of the network for the delocalized (red), multifractal (orange), and localized (purple) phases. Here, the system size is $N = 510$ in all cases.

where the on-site energies $\epsilon_i = [-1/2, 1/2]$ are drawn from a uniform random distribution and Δ is the disorder parameter. Here, J is set as unity.

In Fig. 9(a), we plot the phase diagram of the 3D Anderson model, with increasing strength of disorder Δ and the color denoting the multifractal dimension D_2. Above the critical disorder strength $\Delta \approx 16.5$ [69], all the eigenstates are exponentially localized with D_2 close to zero. At subcritical disorder strengths, localized and extended states are observed, separated by some critical energy, dubbed the mobility edge [70]. We employ the binary classifier by training it on all the eigenstates of the AAH model at the disorder strengths $\lambda = 0.5$ (delocalized phase) and $\lambda = 4$ (localized). The resulting network is then used to predict the phase diagram of the 3D Anderson model, as shown in Fig. 9(b). We observe that the network precisely identifies the delocalized eigenstates with $P \approx 0$, the mobility edges with $0 < P < 1$, separating the delocalized and localized eigenstates as well as the critical disorder strength $\Delta \approx 16.5$ beyond which all the eigenstates are localized with P close to unity. Thus, the network predicts the phase diagram of a system subjected to random disorder with reasonable accuracy despite the fact that it was trained on the eigenstates of a system with a quasiperiodic disorder and whose geometry is set in a different dimension.

APPENDIX B: HIGHER-ORDER FRACTAL DIMENSION

In this section, we utilize higher-order fractal dimension D_6 [see Eq. (9)] to label the eigenstates as delocalized, localized, and multifractal in order to train the neural networks. For each eigenstate, the fractal dimension D_6 is calculated and labeled as follows:

$$\begin{aligned} D_6 &< 0.2, && \text{localized}, \\ 0.2 \leqslant D_6 &\leqslant 0.8, && \text{multifractal}, \\ D_6 &> 0.8, && \text{delocalized}. \end{aligned} \tag{B1}$$

In Figs. 10(a) and 10(c) we have calculated D_6 as a function of disorder strength λ for all the single-particle eigenstates for the long-range hopping parameter $\sigma = 0.5$ and 3.0. The corresponding phase diagrams plotted using the multiclass classification neural network trained using the eigenstates of the LRH model where the class is assigned using D_6 are shown in Figs. 10(b) and 10(d). We next compute the multifractal dimension D_6 as a function of disorder strength λ for all the single-particle eigenstates of the AAH model [see Fig. 10(e)]. The corresponding phase diagram obtained using the neural network trained on the eigenstates of the LRH model is shown in Fig. 10(f). We observe that even when the network is trained on the eigenstates labeled using higher moments, such as D_6, it classifies the various phases with reasonable accuracy, as well as precisely predicts the location of the transitions/steps. This implies that any quantity which reflects the localization properties of the system can be used for labeling data in supervised machine learning.

[1] M. I. Jordan and T. M. Mitchell, Machine learning: Trends, perspectives, and prospects, Science **349**, 255 (2015).

[2] G. Carleo, I. Cirac, K. Cranmer, L. Daudet, M. Schuld, N. Tishby, L. Vogt-Maranto, and L. Zdeborová, Machine learning and the physical sciences, Rev. Mod. Phys. **91**, 045002 (2019).

[3] M. Ippoliti, S. D. Geraedts, and R. N. Bhatt, Connection between Fermi contours of zero-field electrons and $\nu = \frac{1}{2}$ composite fermions in two-dimensional systems, Phys. Rev. B **96**, 045145 (2017).

[4] R. Ramprasad, R. Batra, G. Pilania, A. Mannodi-Kanakkithodi, and C. Kim, Machine learning in materials informatics: Recent applications and prospects, npj Comput. Mater. **3**, 54 (2017).

[5] K. Ch'ng, J. Carrasquilla, R. G. Melko, and E. Khatami, Machine learning phases of strongly correlated fermions, Phys. Rev. X **7**, 031038 (2017).

[6] F. Schindler, N. Regnault, and T. Neupert, Probing many-body localization with neural networks, Phys. Rev. B **95**, 245134 (2017).

[7] S. J. Wetzel and M. Scherzer, Machine learning of explicit order parameters: From the Ising model to SU(2) lattice gauge theory, Phys. Rev. B **96**, 184410 (2017).

[8] S. J. Wetzel, Unsupervised learning of phase transitions: From principal component analysis to variational autoencoders, Phys. Rev. E **96**, 022140 (2017).

[9] L. Wang, Discovering phase transitions with unsupervised learning, Phys. Rev. B **94**, 195105 (2016).
[10] Y.-H. Liu and E. P. L. van Nieuwenburg, Discriminative cooperative networks for detecting phase transitions, Phys. Rev. Lett. **120**, 176401 (2018).
[11] P. Broecker, F. F. Assaad, and S. Trebst, Quantum phase recognition via unsupervised machine learning, arXiv:1707.00663.
[12] W. Hu, R. R. P. Singh, and R. T. Scalettar, Discovering phases, phase transitions, and crossovers through unsupervised machine learning: A critical examination, Phys. Rev. E **95**, 062122 (2017).
[13] T. Cadez, B. Dietz, D. Rosa, A. Andreanov, K. Slevin, and T. Ohtsuki, Machine learning wave functions to identify fractal phases, arXiv:2306.01402.
[14] J. Liu, Y. Qi, Z. Y. Meng, and L. Fu, Self-learning Monte Carlo method, Phys. Rev. B **95**, 041101(R) (2017).
[15] L. Huang and L. Wang, Accelerated Monte Carlo simulations with restricted Boltzmann machines, Phys. Rev. B **95**, 035105 (2017).
[16] L. Wang, Exploring cluster Monte Carlo updates with Boltzmann machines, Phys. Rev. E **96**, 051301(R) (2017).
[17] G. Carleo and M. Troyer, Solving the quantum many-body problem with artificial neural networks, Science **355**, 602 (2017).
[18] I. Glasser, N. Pancotti, M. August, I. D. Rodriguez, and J. I. Cirac, Neural-network quantum states, string-bond states, and chiral topological states, Phys. Rev. X **8**, 011006 (2018).
[19] S. Lu, X. Gao, and L.-M. Duan, Efficient representation of topologically ordered states with restricted Boltzmann machines, Phys. Rev. B **99**, 155136 (2019).
[20] G. Carleo, Y. Nomura, and M. Imada, Constructing exact representations of quantum many-body systems with deep neural networks, Nat. Commun. **9**, 5322 (2018).
[21] G. Torlai, G. Mazzola, J. Carrasquilla, M. Troyer, R. Melko, and G. Carleo, Neural-network quantum state tomography, Nat. Phys. **14**, 447 (2018).
[22] Z. Cai and J. Liu, Approximating quantum many-body wave functions using artificial neural networks, Phys. Rev. B **97**, 035116 (2018).
[23] B. Gardas, M. M. Rams, and J. Dziarmaga, Quantum neural networks to simulate many-body quantum systems, Phys. Rev. B **98**, 184304 (2018).
[24] J. Carrasquilla and G. Torlai, How to use neural networks to investigate quantum many-body physics, PRX Quantum **2**, 040201 (2021).
[25] M. Schmitt and M. Heyl, Quantum many-body dynamics in two dimensions with artificial neural networks, Phys. Rev. Lett. **125**, 100503 (2020).
[26] P. Cunningham, M. Cord, and S. J. Delany, Supervised learning, in *Machine Learning Techniques for Multimedia*, edited by M. Cord and P. Cunningham (Springer, Berlin, Heidelberg, 2008), pp. 21–49.
[27] P. Broecker, J. Carrasquilla, R. G. Melko, and S. Trebst, Machine learning quantum phases of matter beyond the fermion sign problem, Sci. Rep. **7**, 8823 (2017).
[28] Y. Zhang and E.-A. Kim, Quantum loop topography for machine learning, Phys. Rev. Lett. **118**, 216401 (2017).
[29] T. Ohtsuki and T. Ohtsuki, Deep learning the quantum phase transitions in random two-dimensional electron systems, J. Phys. Soc. Jpn. **85**, 123706 (2016).
[30] P. Zhang, H. Shen, and H. Zhai, Machine learning topological invariants with neural networks, Phys. Rev. Lett. **120**, 066401 (2018).
[31] P. W. Anderson, Absence of diffusion in certain random lattices, Phys. Rev. **109**, 1492 (1958).
[32] A. I. Goldman and R. F. Kelton, Quasicrystals and crystalline approximants, Rev. Mod. Phys. **65**, 213 (1993).
[33] M. Kohmoto, B. Sutherland, and C. Tang, Critical wave functions and a cantor-set spectrum of a one-dimensional quasicrystal model, Phys. Rev. B **35**, 1020 (1987).
[34] A. Ahmed, N. Roy, and A. Sharma, Dynamics of spectral correlations in the entanglement Hamiltonian of the Aubry-André-Harper model, Phys. Rev. B **104**, 155137 (2021).
[35] A. Ahmed, A. Ramachandran, I. M. Khaymovich, and A. Sharma, Flat band based multifractality in the all-band-flat diamond chain, Phys. Rev. B **106**, 205119 (2022).
[36] A. Ahmed, N. Roy, and A. Sharma, Interplay of many-body interactions and quasiperiodic disorder in the all-bands-flat diamond chain, Phys. Rev. B **107**, 245110 (2023).
[37] S. Aubry and G. André, Analyticity breaking and Anderson localization in incommensurate lattices, Ann. Israel Phys. Soc. **3**, 18 (1980).
[38] P. G. Harper, Single band motion of conduction electrons in a uniform magnetic field, Proc. Phys. Soc., Sect. A **68**, 874 (1955).
[39] R. P. A. Lima, H. R. da Cruz, J. C. Cressoni, and M. L. Lyra, Finite-size scaling of power-law bond-disordered Anderson models, Phys. Rev. B **69**, 165117 (2004).
[40] A. D. Mirlin, Y. V. Fyodorov, F.-M. Dittes, J. Quezada, and T. H. Seligman, Transition from localized to extended eigenstates in the ensemble of power-law random banded matrices, Phys. Rev. E **54**, 3221 (1996).
[41] X. Deng, V. E. Kravtsov, G. V. Shlyapnikov, and L. Santos, Duality in power-law localization in disordered one-dimensional systems, Phys. Rev. Lett. **120**, 110602 (2018).
[42] X. Deng, S. Ray, S. Sinha, G. V. Shlyapnikov, and L. Santos, One-dimensional quasicrystals with power-law hopping, Phys. Rev. Lett. **123**, 025301 (2019).
[43] S. Gopalakrishnan, Self-dual quasiperiodic systems with power-law hopping, Phys. Rev. B **96**, 054202 (2017).
[44] N. Roy and A. Sharma, Fraction of delocalized eigenstates in the long-range Aubry-André-Harper model, Phys. Rev. B **103**, 075124 (2021).
[45] M. Janssen, Multifractal analysis of broadly-distributed observables at criticality, Int. J. Mod. Phys. B **08**, 943 (1994).
[46] M. Schreiber and H. Grussbach, Multifractal wave functions at the Anderson transition, Phys. Rev. Lett. **67**, 607 (1991).
[47] A. Brezini, Localization in one-dimensional random potential, Phys. Status Solidi B **128**, K81 (1985).
[48] J. L. Beeby and N. F. Mott, The electronic structure of disordered system, Proc. R. Soc. London A **279**, 82 (1964).
[49] O. Bohigas, M. J. Giannoni, and C. Schmit, Characterization of chaotic quantum spectra and universality of level fluctuation laws, Phys. Rev. Lett. **52**, 1 (1984).
[50] M. Modugno, Exponential localization in one-dimensional quasi-periodic optical lattices, New J. Phys. **11**, 033023 (2009).
[51] F. Evers and A. D. Mirlin, Anderson transitions, Rev. Mod. Phys. **80**, 1355 (2008).
[52] D. J. Thouless, Bandwidths for a quasiperiodic tight-binding model, Phys. Rev. B **28**, 4272 (1983).

[53] W. S. McCulloch and W. Pitts, A logical calculus of the ideas immanent in nervous activity, Bull. Math. Biophys. **5**, 115 (1943).

[54] F. Rosenblatt, The perceptron: A probabilistic model for information storage and organization in the brain, Psychological Rev. **65**, 386 (1958).

[55] C. M. Bishop, *Pattern Recognition and Machine Learning* (Springer-Verlag, Berlin, Heidelberg, 2006).

[56] S. R. Dubey, S. K. Singh, and B. B. Chaudhuri, Activation functions in deep learning: A comprehensive survey and benchmark, arXiv:2109.14545.

[57] I. J. Goodfellow, Y. Bengio, and A. Courville, *Deep Learning* (MIT Press, Cambridge, MA, 2016).

[58] N. Srivastava, G. Hinton, A. Krizhevsky, I. Sutskever, and R. Salakhutdinov, Dropout: A simple way to prevent neural networks from overfitting, J. Mach. Learn. Res. **15**, 1929 (2014).

[59] K. Fukushima, Cognitron: A self-organizing multilayered neural network, Biol. Cybernetics **20**, 121 (1975).

[60] J. Feng and S. Lu, Performance analysis of various activation functions in artificial neural networks, J. Phys.: Conf. Ser. **1237**, 022030 (2019).

[61] A. F. Agarap, Deep learning using rectified linear units (relu), arXiv:1803.08375.

[62] D. E. Rumelhart, G. E. Hinton, and R. J. Williams, Learning representations by back-propagating errors, Nature (London) **323**, 533 (1986).

[63] D. P. Kingma and J. Ba, Adam: A method for stochastic optimization, arXiv:1412.6980.

[64] Y. Song, A. G. Schwing, R. S. Zemel, and R. Urtasun, Training deep neural networks via direct loss minimization, arXiv:1511.06411.

[65] J. Lindinger, A. Buchleitner, and A. Rodríguez, Many-body multifractality throughout bosonic superfluid and Mott insulator phases, Phys. Rev. Lett. **122**, 106603 (2019).

[66] N. Macé, F. Alet, and N. Laflorencie, Multifractal scalings across the many-body localization transition, Phys. Rev. Lett. **123**, 180601 (2019).

[67] Y. Wang, Y. Wang, and S. Chen, Spectral statistics, finite-size scaling and multifractal analysis of quasiperiodic chain with p-wave pairing, Eur. Phys. J. B **89**, 254 (2016).

[68] M. Abadi, A. Agarwal, P. Barham, E. Brevdo, Z. Chen, C. Citro, G. Corrado, A. Davis, J. Dean, M. Devin, S. Ghemawat, I. Goodfellow, A. Harp, G. Irving, M. Isard, Y. Jia, R. Jozefowicz, L. Kaiser, M. Kudlur, J. Levenberg *et al.*, Tensorflow: Large-scale machine learning on heterogeneous distributed systems (2015), http://download.tensorflow.org/paper/whitepaper2015.pdf.

[69] N. F. Mott, Conduction in glasses containing transition metal ions, J. Non-Cryst. Solids **1**, 1 (1968).

[70] T. Brandes and S. Kettemann, editors, *Anderson Localization and Its Ramifications: Disorder, Phase Coherence, Electron Correlations* (Springer, 2003).